INTERNATIONAL JOURNAL FOR NUMERICAL METHODS IN FLUIDS, VOL. 5, 311–329 (1985)

NUMERICAL AND EXPERIMENTAL STUDY OF DRIVEN FLOW IN A POLAR CAVITY

L. FUCHS AND N. TILLMARK

Department of Gasdynamics, The Royal Institute of Technology, Stockholm, Sweden

SUMMARY

A numerical and an experimental study of the flow of an incompressible fluid in a polar cavity is presented. The experiments included flow visualization, in two perpendicular planes, and quantitative measurements of the velocity field by a laser Doppler anemometer. Measurements were done for two ranges of Reynolds numbers; about 60 and about 350. The stream function–vorticity form of the governing equations was approximated by upwind or central finite-differences. Both types of finite-difference approximations were solved by a multi-grid method. Numerical solutions were computed on a sequence of grids and the relative accuracy of the solutions was studied. Our most accurate numerical solutions had an estimated error of 0·1 per cent and 1 per cent for $Re = 60$ and $Re = 350$, respectively. It was also noted that the solution to the second order finite difference equations was more accurate, compared to the solution to the first order equations, only if fine enough meshes were used. The possibility of using extrapolations to improve accuracy was also considered. Extrapolated solutions were found to be valid only if solutions computed on fine enough meshes were used. The numerical and the experimental results were found to be in very good agreement.

KEY WORDS Cavity Flows Finite-differences Numerical Accuracy Velocity Measurements

INTRODUCTION

The computation of the flow in a driven cavity has been used as a standard problem to test numerical methods for incompressible flows. A review of many of these methods and a comparison of some parameters are given by Tuann and Olson,[1] Gupta and Manohar[2] and Peyret and Taylor.[3] In most published works the computed flow field is characterized by the streamline pattern and by the equi-vorticity line pattern, the values of the stream function and the vorticity at the centre of the main vortex and, in some cases, the location of that point.

The comparison of these numerical parameters leads to the following observations: The (qualitative) streamline patterns are similar for different methods. On the other hand the numerical values of the stream function and the vorticity at the centre of the main vortex reveal some differences (see e.g. Table III of Reference 2). We also note that the numerical solution for a given Reynolds number (*Re*) is sensitive to the form of the partial differential equations (PDE) (conservative or non-conservative forms) and to the formal order of accuracy of the finite-difference approximations. Unfortunately, the formal accuracy does not tell how accurate the solution is, for a given mesh. This is so since the truncation errors indicate the asymptotic behaviour of the finite-difference equations (FDE) and the solution to it, as the mesh size goes to zero. When the PDE has a unique solution the asymptotic numerical solution should give an accurate description of the real flow. It has been observed recently[4] that for a given mesh and for a certain range of *Re* (which depends on the mesh) the FDE may have non-unique solutions, and these solutions are not 'close' to the solution which is obtained on a much finer grid. This fact emphasizes the importance of

0271–2091/85/040311–19$01.90

Received 7 December 1983
Revised 12 June 1984

quantitative experimental data which can be used in the assessment of the accuracy of numerical methods and in choosing the 'right' solution in cases of non-uniqueness.

It is remarkable that in contrast to the numerous numerical solutions to the driven cavity problem, there is only very limited experimental information on such flows. Pan and Acrivos[5] published a flow visualization study of the flow in rectangular cavities and Reynolds numbers up to 2700. Their apparatus consisted of a 12-inch-diameter wheel rotating on top of a hole of 40 inch depth and 4 × 4-inch cross-section. The hole was fitted with a removable diaphragm to adjust the desired aspect ratio (height to width ratio). Mills'[6] experiments were conducted on a square cavity. The flow in the cavity was visualized and some measured data were obtained by a hot-wire anemometer, for $Re = 10^5$. All these results, unfortunately, cannot be used as reference for detailed quantitative comparisons with numerical solutions.

In recent years some laser Doppler velocity measurements on a channel-flow driven[7] and a lid-driven[8] cavity have been reported. Bogatyrev and Gorin[7] studied the flow in a rectangular (3-D) cavity. The upper wall of the cavity was open to a straight channel. The flow in the cavity was driven by the motion of the fluid in the channel. The results of these measurements cannot be used for comparison with numerical solutions for the lid-driven cavity. More relevant results for the lid-driven cavity were presented by Kossef *et al.*[8] Their cavity had a square cross-section and length to depth ratio of 3:1 and 1:1 ($10^3 \leq Re \leq 10^4$). In all cases no steady 2-D flow was present.

Here, we treat the flow in a polar cavity (this geometry has been chosen for experimental reasons). The governing equations for two-dimensional viscous flows are written in terms of the stream function and the vorticity, in polar co-ordinates. The discretized problem is solved by a multigrid (MG) method. The accuracy of the numerical solutions is studied and extrapolated results are computed. The numerical solutions are compared with our experimental results for the available cases.

Our experiments had two purposes. First, to give a qualitative description of the flow field (including the secondary vortices) by flow visualization and secondly, to provide the velocity vector along some radial lines. The measurements were done by a laser-Doppler anemometer for two *Re*

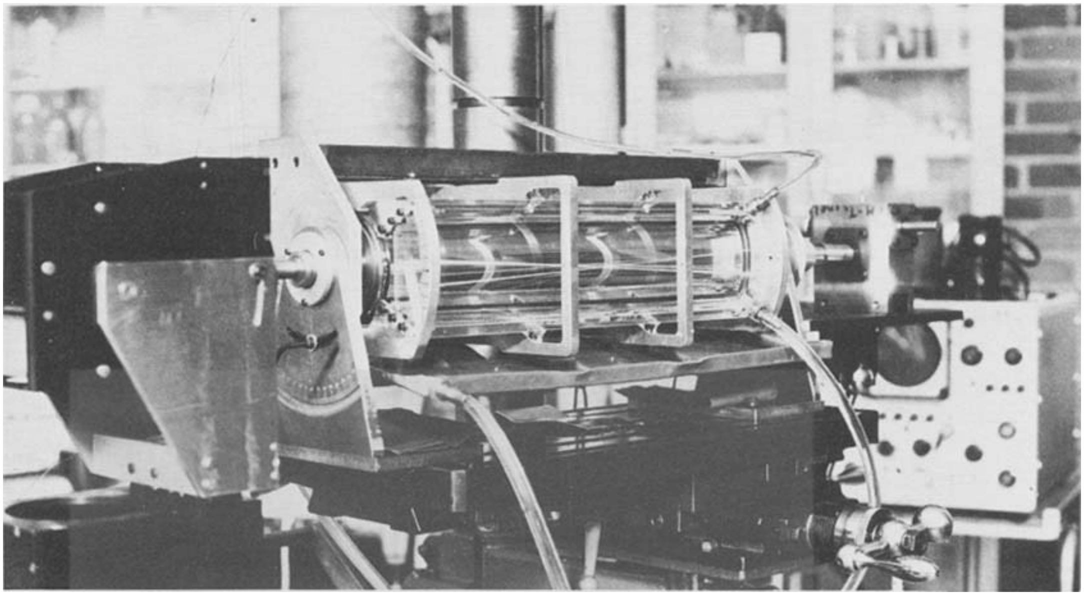

Figure 1(a). The experimental configuration groups ('low' *Re* about 60 and 'high' *Re* about 350). For the higher *Re* group three-dimensional flow was observed in the entire cavity and for increasing *Re* more and more air-bubbles were mixed into the fluid. For these reasons no measurements were done for higher Reynolds numbers.

NUMERICAL SIMULATION OF THE FLOW

The governing equations and their approximation

The numerical simulation of the flow in an apparatus of the type shown in Figure 1(a) is considered. Here, we assume a two-dimensional flow in the plane, normal to the axis of the cylindrical cavity.

The Navier–Stokes equations are written in polar co-ordinates (r, θ) in terms of the stream function (ψ) and the vorticity (ω) as dependent variables.

$$\nabla^2 \omega - Re\left(u\omega_r + \frac{v}{r}\omega_\theta \right) = 0 \tag{1}$$

$$\nabla^2 \psi - \omega = 0 \tag{2}$$

where

$$\nabla^2 q = \frac{1}{r}(rq_r)_r + \frac{1}{r^2} q_{\theta\theta}$$

$$u = \frac{1}{r}\psi_\theta, \quad v = -\psi_r$$

with u and v as the radial and the azimuthal components of the velocity vector, respectively. The Reynolds number, *Re*, is based upon the radius, the surface-velocity of the rotating cylinder which drives the flow, and the kinematic viscosity of the fluid.

The computational geometry is displayed in Figure 1(b). The no-slip boundary conditions are applied on the solid walls. The walls of the driven cavity give rise to a closed streamline. The no-slip boundary conditions specify also the normal derivative of the stream function. This derivative, together with equation (2) can be used to compute the boundary vorticity.

A polar mesh with uniform spacing in both the radial and the azimuthal directions, is used. The differential equation (1) and (2) are approximated by second order accurate central differences. The

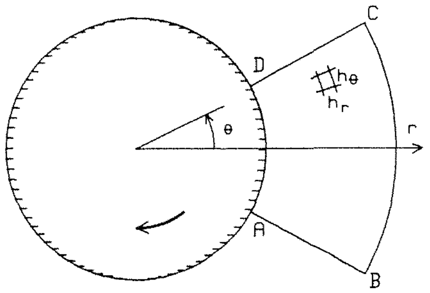

Figure 1(b). The two-dimensional cavity, the polar co-ordinates and the computational domain ABCD. The boundary DA moves with a constant velocity which is used in defining the Reynolds number. The radius of the rotating cylinder is taken as the reference length convective terms are approximated by first order accurate upwind differences ($\overleftrightarrow{\partial}_r$, $\overleftrightarrow{\partial}_\theta$) or central differences (∂_r, ∂_θ):

$$\nabla_h^2 \omega - Re\left(u\tilde{\partial}_r + \frac{v}{r}\tilde{\partial}_\theta\right)\omega = 0 \tag{3}$$

$$\nabla_h^2 \psi - \omega = 0 \tag{4}$$

where ∇_h^2 is a second order accurate central difference approximation to ∇^2. $\tilde{\partial}_r$ and $\tilde{\partial}_\theta$ denote either the upwind or the central finite-difference operator in the r and θ directions, respectively.

The boundary conditions are as follows: $\psi = 0$ on the boundary ABCD (in Figure 1(b)). The boundary vorticity is computed by the following finite-difference relations:

Along AB:

$$\omega_{i,1} = 2\psi_{i,2}/r_1^2 h_\theta^2 \tag{5a}$$

along BC:

$$\omega_{I,j} = 2r_{I-1/2}\psi_{I-1,j}/r_I h_r^2 \tag{5b}$$

along CD:

$$\omega_{i,J} = 2\psi_{i,J-1}/r_i^2 h_\theta^2 \tag{5c}$$

along DA:

$$\omega_{1,j} = 2(r_{3/2}\psi_{2,j}/r_1 + h_r)/h_r^2 \tag{5d}$$

The system of finite-difference equations (3), (4) and (5) can be solved by different iterative methods.[9] Here, we describe shortly a multi-grid method which, because of its efficiency, has been used in all our numerical computations.

Multi-grid solution of the FDE

In all our computations we have used a simplified version of the MG method of Thunell and Fuchs.[10] In the following we discuss briefly some of the details of the method and indicate possible improvements to increase the computational efficiency.

The smoothing in the MG scheme is done by a point relaxation method. At each node point both ω and ψ are updated, in such a way that equations (3) and (4) are satisfied locally. The direction of the relaxation sweep is from corner A toward corner C in Figure 1(b). As shown by Fuchs[11] there are several factors which determine the smoothing efficiency. Among these factors are the mesh spacing ratio (rh_θ/h_r) and the alignment of the directions of the relaxation and the flow. Optimal smoothing is obtained when the mesh spacing ratio equals one and, for large Re, if the relaxation is done in the flow direction. In our case the mesh spacing ratio varies between 1 and 2, and the relaxation direction is against the flow in a substantial part of the flow field. However, even the simple, non-optimal, relaxation scheme gives an acceptable smoothing of high frequency error components.

Injection is used as dependent variable transfer (restriction) operator from fine to coarse grids. That is, the values of the dependent variables are the same on all nodal points which are in common for the different grids. By using averaging, a smoothing effect is achieved and faster convergence can be obtained.[10]

For the square cavity, Thunell and Funchs[10] have also shown that the choice of the boundary vorticity approximation and its application, affects the total convergence rate of the MG scheme.

Further improvements could be achieved by using a weighted Jacobi relaxation scheme. Here, we made no attempts to optimize the different MG steps. In spite of the fact that the method was not optimal, relatively fast convergence was obtained for a wide range of *Re*.

EXPERIMENTAL APPARATUS AND TECHNIQUES

The apparatus consists of a cylinder and a cylindrical cavity with parallel end walls and a cricle-sector cross-section (see Figure 1(a)). The circle sector is limited towards the apex by the cylinder surface, and the distant wall is a fixed circle bow. The cylinder has a diameter of 95 mm and the length of the cavity is 400 mm. The radial walls are 47·5 mm high and the opening angle is 1 radian. The cylinder is made of chromium-plated steel and the walls of plexiglass. It is possible to turn the cylindrical cavity around its axis, and to fix it at different angles. A cylindrical co-ordinate system (r, θ, Z) is used in such a way that the axis of the rotating cylinder is parallel with the Z-axis. The end wall of the apparatus through which the laser beams enter the cavity, is at $Z = 0$.

The cavity was filled with Shell Ondina-oil 32 ($\nu = 8 \times 10^{-5}\,\mathrm{m^2/s}$ at 20°C) through a hole in the far end bottom corner, while another hole located near the top corner, was used for air ventilation. The latter hole was also used as passage for a thermocouple to check the oil temperature. An a.c. motor rotated the cylinder at a measured rate. The apparatus was placed on a machine base to allow vertical and horizontal adjustments.

The velocity field was measured with a laser Doppler anemometer (LDA) in backscatter mode. The LDA consists of DISA-55X modular LDA optics, traversing system, counter, frequency shifter, a Digital PDP 11/05 computer, a 4 W Ar-ion laser and a home-made channel switch. As the laser beams penetrated through the end wall, the traversing system made it possible to move the measuring volume in a radial direction. Using a lens of focal length 310 mm and a beam-expansion ratio of 1·9, the measuring volume was estimated to be 1·1 mm long and 0·88 mm in diameter. The oil was seeded with Al_2O_3 particles (less than 2·5 μm in diameter).

The traversing and the switching between channels were computer controlled. At each measuring point, 50 samples were taken per velocity component and the mean velocity for each component was computed by the 'residence time weighting' method,[12] The velocity field in three different cross-sections ($Z = 10$, $Z = 100$ and $Z = 200$ mm) was measured. Measurements were made for two ranges of Reynolds number: The 'low' *Re* range was about 60, and the 'high' *Re* range was about 350. The measurements in the middle plane ($Z = 200$ mm) were more restricted in angle and the sampling times were long (several seconds), therefore most results which are given here are for the measurements in the plane $Z = 100$ mm.

A flow visualization technique was also used to produce a qualitative picture of the flow field. By this method, some three-dimensional effects were estimated. The flow field was visualized by using Al_2O_3 particles. By letting a narrow laser beam pass through a glass rod, a thin slice of the cylindrical cavity was illuminated. Pictures at some different stations were taken for the two *Re* groups.

NUMERICAL AND EXPERIMENTAL RESULTS

Numerical results

First, we consider the efficiency of the MG method which is described above. We define a work unit as the computational effort which is equivalent to one relaxation sweep on the finest grid. The average convergence factor, η, is defined as:

$$\eta = \left[\frac{\| R_\mathrm{f} \|}{\| R_\mathrm{i} \|}\right]^{1/W} \tag{6}$$

where R_f and R_i are the final and the initial residuals, respectively, and W is the number of work units which is needed to attain R_f.

Table I shows the average convergence factors of the MG method for different numbers of mesh intervals, N, (in the finest grid) and some Re. The coarsest grid in all cases is the same (with 4 × 4 intervals).

The convergence factor on the fine grids turned out to be insensitive to variations in the Reynolds number for $Re \leqslant 2000$. For coarse grids, the convergence is fast only for relatively small Reynolds numbers.

The convergence factors of the present method are not as good as those which are given by Thunell and Funchs[10] for the square cavity problem. On the other hand the current method can be considered as efficient: by a computational effort roughly equal to about 100 relaxation sweeps on the finest grid, the residuals are reduced by 6 orders of magnitudes for all $Re \leqslant 500$.

Results were computed on different grids and $Re \leqslant 2000$. The iterations were terminated when the residuals of equations (3) and (4) became less than 10^{-6}. This high accuracy is much beyond (by several orders of magnitudes) the truncation errors. On the other hand, high accuracy in solving the FDE is needed if extrapolations are to be meaningful. For $Re = 350$ and $Re = 60$ numerical solutions were computed on several grids (with the finest containing 128 × 128 intervals). For other Re, most results were computed on a medium grid with 80 × 80 intervals.

To gain some information about the accuracy of the numerical solutions, we have solved the FDE for $Re = 60$ and $Re = 350$ on successively refined grids. Assuming that the order of accuracy of the solution is n, then the following expansions are valid:

$$\begin{aligned} \psi_h &= \tilde{\psi} + h^n p_1 + h^{n+1} p_2 + \cdots \\ u_h &= \tilde{u} + h^n q_1 + h^{n+1} q_2 + \cdots \\ v_h &= \tilde{v} + h^n r_1 + h^{n+1} r_2 + \cdots \\ \omega_h &= \tilde{\omega} + h^n s_1 + h^{n+1} s_2 + \cdots \end{aligned} \tag{7}$$

where p_i, q_i, r_i, and s_i are truncation error functions. $\tilde{\psi}$, $\tilde{u}$, $\tilde{v}$ and $\tilde{\omega}$ solve the differential problem (1) and (2). If the assumption on the accuracy is correct, then these functions are independent of h. The

Table I. The convergence factor, η, for some grids and Re

Re	$N = 16$	$N = 32$	$N = 64$
10	0·76	0·82	0·84
60	0·76	0·80	0·85
350	0·89	0·88	0·87
500	0·89	0·91	0·87
750	—	0·91	0·88
1000	0·96	0·91	0·90
1500	—	0·95	0·90
2000	—	—	0·90

validity of the assumption may be checked by computing p_1, q_1, r_1 and s_1 in the following way:

$$\tau_1^{i,j} = (t_i - t_j)/(h_i^n - h_j^n) \tag{8}$$

where t and τ stand for ψ, u, v or ω and p, q, r or s, respectively.

The truncation error functions are computed by using the finest grid as reference ($j = 1$). The root mean square values of the computed p_1, q_1, r_1 and s_1 for the solution to the upwind FDE ($n = 1$) on some grid combinations and $Re = 350$, are displayed in Table II.

Table II shows that the truncation error functions are (almost) independent of the mesh size. This fact indicates that expansion (7) is valid and extrapolated solutions may be computed by using the solutions obtained on different grids (finer than 32 × 32 intervals for $Re = 350$).

It is also noted that the absolute values of these truncation error functions increase with increasing order of derivation of ψ (i.e. $|s_1| > |q_1| > |p_1|$). This means that the different terms in expansions (7) are not represented by their coefficients unless h is small enough. Under such circumstances a formally second (or higher) order scheme does not give better accuracy than the one obtained by the first order method on relatively coarse grids. For the same reason the accuracy of extrapolated results based upon coarse grid solutions may be even less accurate than the original solutions. To be able to determine the coarsest grid which may be used for extrapolation purposes, the truncation error functions have to be computed.

The accuracy levels of the numerical solutions have been studied by considering the values of the stream function on a group of mesh points in common to a sequence of grids. This group of mesh points includes 81 nodal points, uniformly distributed in the cavity. Extrapolated values of the stream functions (ψ^e) at these points are computed. The relative error can be defined, for the solution (ψ_j) on each grid j, by

$$e_j = \|\psi^e - \psi_j\| / \|\psi^e\|$$

Figures 2 and 3 show the relative error as a function of the mesh size ($1/N$) for $Re = 60$ and $Re = 350$, respectively. The computed order of convergence has been defined by the slope of the best (RMS) straight-line fit through data related to grids with more than 48 intervals in each direction. As seen, the asymptotic rate of convergence, as N increases, is as predicted by the theory for both finite difference schemes. Furthermore, it is noted that the second order method gives higher

Table II. The truncation error functions computed by relation (8).

$p_1^{2,1} = 1{\cdot}09$	$q_1^{2,1} = 4{\cdot}37$	$r_1^{2,1} = 5.37$	$s_1^{2,1} = 116$
$p_1^{3,1} = 1{\cdot}10$	$q_1^{3,1} = 4{\cdot}43$	$r_1^{3,1} = 5{\cdot}32$	$s_1^{3,1} = 118$
$p_1^{4,1} = 1{\cdot}13$	$q_1^{4,1} = 4{\cdot}50$	$r_1^{4,1} = 5{\cdot}25$	$s_1^{4,1} = 119$
$p_1^{5,1} = 1{\cdot}17$	$q_1^{5,1} = 4{\cdot}58$	$r_1^{5,1} = 5{\cdot}10$	$s_1^{5,1} = 119$
$p_1^{6,1} = 1{\cdot}19$	$q_1^{6,1} = 4{\cdot}60$	$r_1^{6,1} = 4{\cdot}98$	$s_1^{6,1} = 116$
$p_1^{7,1} = 1{\cdot}22$	$q_1^{7,1} = 4{\cdot}56$	$r_1^{7,1} = 4{\cdot}77$	$s_1^{7,1} = 108$
$p_1^{8,1} = 1{\cdot}19$	$q_1^{8,1} = 4{\cdot}25$	$r_1^{8,1} = 4{\cdot}34$	$s_1^{8,1} = 88$
$p_1^{9,1} = 1{\cdot}02$	$q_1^{9,1} = 3{\cdot}88$	$r_1^{9,1} = 3{\cdot}53$	$s_1^{9,1} = 70$

The superscripts denote the following grids:
1: 128 × 128 intervals, 2: 96 × 96 intervals
3: 80 × 80 intervals, 4: 64 × 64 intervals
5: 48 × 48 intervals, 6: 40 × 40 intervals
7: 32 × 32 intervals, 8: 24 × 24 intervals
9: 16 × 16 intervals.

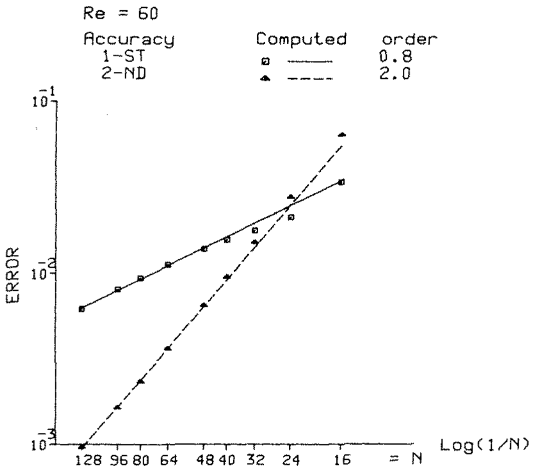

Figure 2. The relative error in the stream function as function of the mesh size (1/N). Upwind (————) and central (------) FDE. $Re = 60$

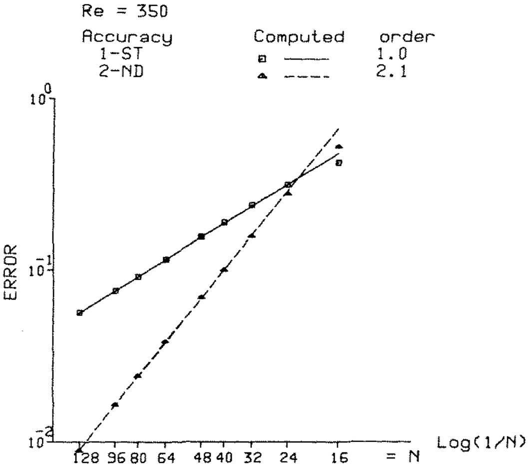

Figure 3. The relative error in the stream function as function of the mesh size (1/N). Upwind (————) and central (-----) FDE. $Re = 350$

level of accuracy only if fine enough meshes are used. The relative error for $Re = 350$ is larger by an order of magnitude compared to the error for $Re = 60$. The error in the numerical solutions which are compared with experimental results in the following, is estimated to about 1 per cent.

An alternative method to higher order finite differences, is to compute an extrapolated solution (e.g. Reference 13). When relations (7) are valid one can eliminate $\tau_1, \tau_2, \ldots, \tau_n$ by using n solutions. However, for $Re = 350$ we have found that extrapolated solutions, obtained by two pairs of solutions result in an indistinguishable streamline pattern. A comparison of the velocity profiles of the extrapolated solution to second and third order accuracy show that the differences are also very small. On the other hand, extrapolation of solutions from coarse grids are inaccurate, which is not unexpected in the light of the truncation error functions variation for coarse grids (Table II).

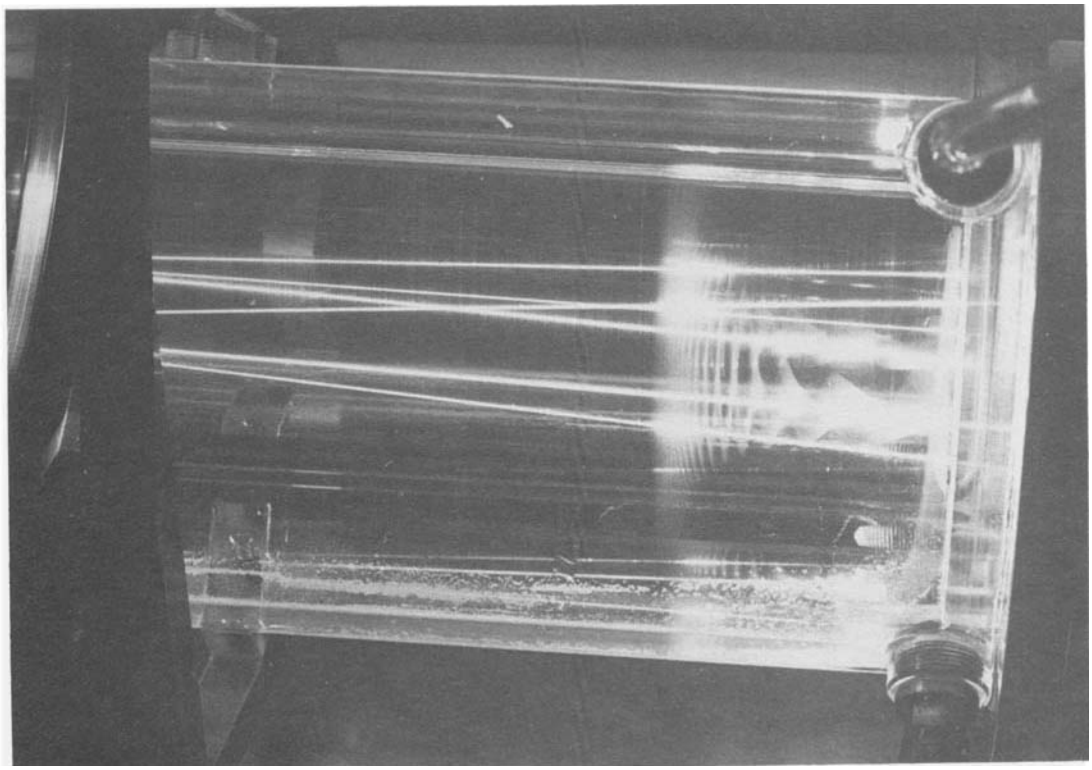

Figure 4. Visualization of the flow in the axial direction. $Re = 55$. The axial velocity component disappears at about 50 mm from the end wall

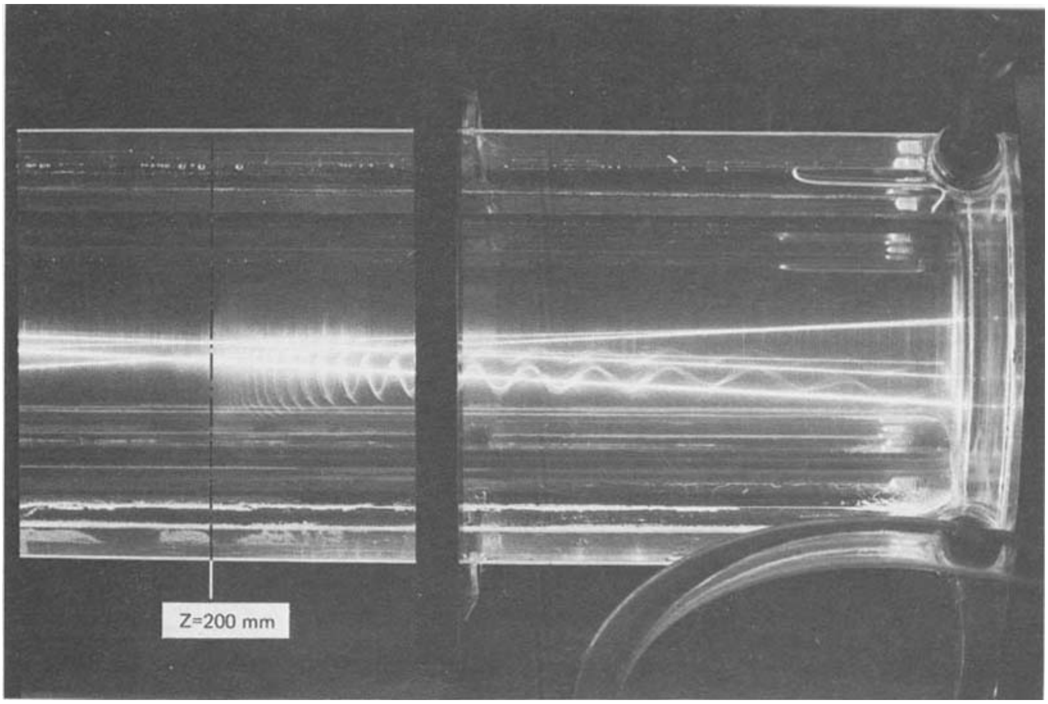

Figure 5. Visualization of the flow in the axial direction. $Re = 350$. The axial velocity component is non-vanishing throughout the cylindrical cavity. Three-dimensional effects are least in the middle of the apparatus ($Z = 200$ mm)

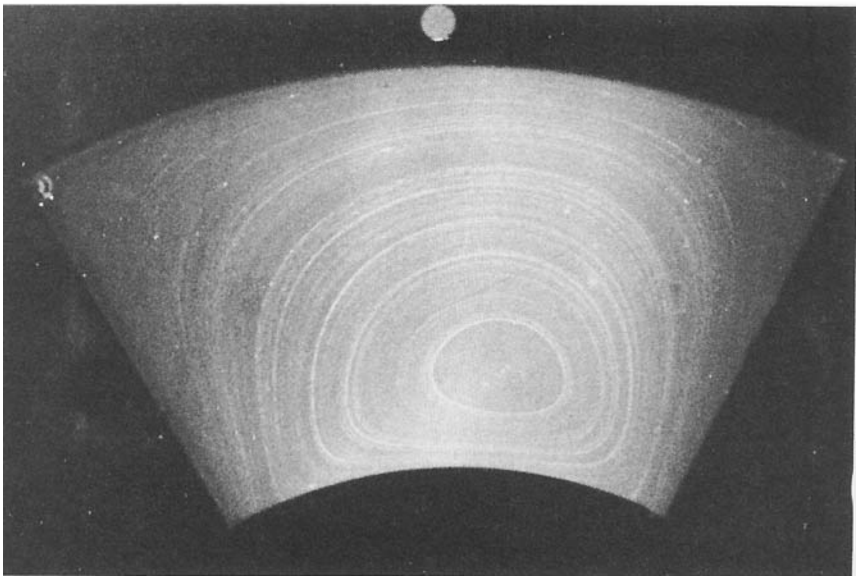

Figure 6. Visualization of the flow in a plane (Z = 100 mm) perpendicular to the axis of the cylindrical cavity. *Re* = 55

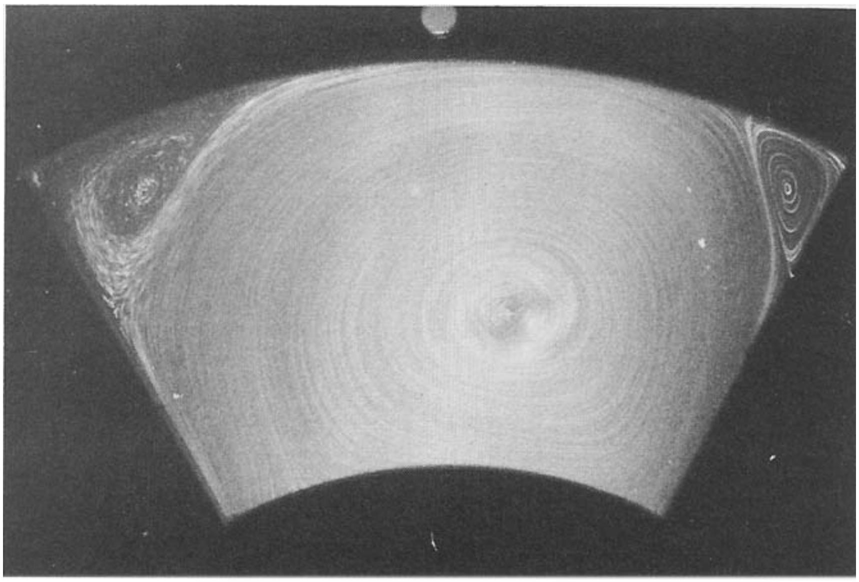

Figure 7. Visualization of the flow in a plane (Z = 100 mm) perpendicular to the axis of the cylindrical cavity. *Re* = 350

Comparison of the numerical and the experimental results

The flow field was visualized by using Al_2O_3 particles. By illuminating heavily seeded oil injected at the filling hole, the axial flow could be seen. Figures 4 and 5 show this axial flow for $Re = 55$ and $Re = 350$, respectively. As seen, the axial flow component persists only in a smaller part of the cylindrical cavity for the low Re. For $Re = 350$, the axial component reaches the middle of the apparatus. Since most of our measurements have been made in a plane ($Z = 100$ mm) where axial flow could be observed (for the high Re group), some deviation from plane flow is unavoidable due to this three-dimensional effect. Pictures of the flow field in three cross-sections have been taken. Figures 6 and 7 show the visualized streamlines, at a plane $Z = 100$ mm, for $Re = 55$ and $Re = 350$, respectively. The numerically computed streamlines for four Reynolds numbers ($Re = 60$, 350, 1000 and 2000) are shown in Figures 8–11. From the streamline pattern some quantitative data on the flow field may be obtained. For $Re = 350$, we measured (from figure 7) the location of the centre of the main vortex with respect to the corners of the cavity and the sizes of the secondary eddies. Comparing these values with those obtained by numerical computations (Figure 9) show that the disagreement is less than 5 per cent. These small differences may be attributed mainly to inaccuracies in the measurements.

The experimental velocity measurements were made along radial lines for nine different angles

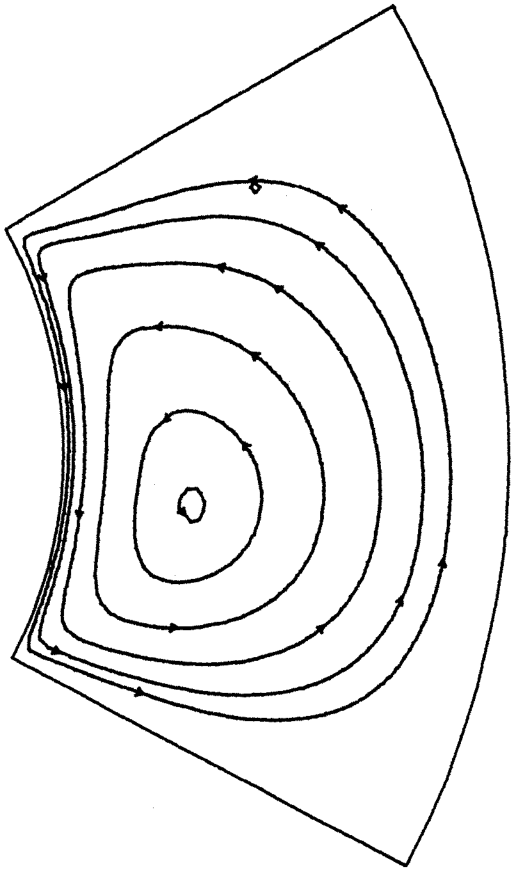

Figure 8. Computed streamline pattern for $Re = 60$ on an 80×80 mesh. Second order

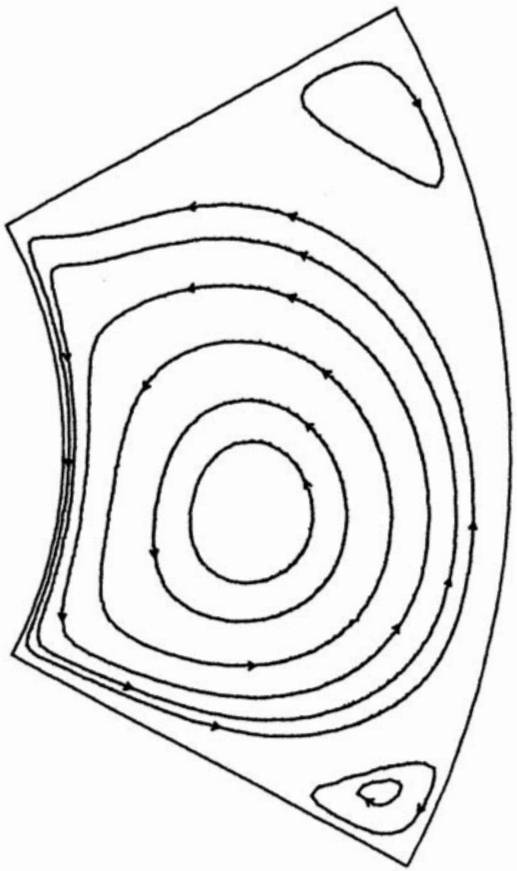

Figure 9. Computed streamline pattern for $Re = 350$ on an 80 × 80 mesh. Second order

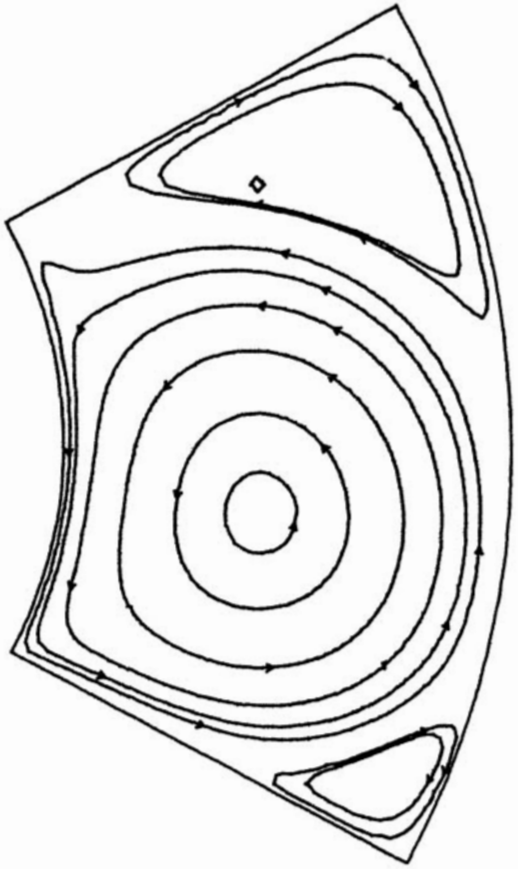

Figure 10. Computed streamline pattern for $Re = 1000$ on an 80 × 80 mesh. Second order

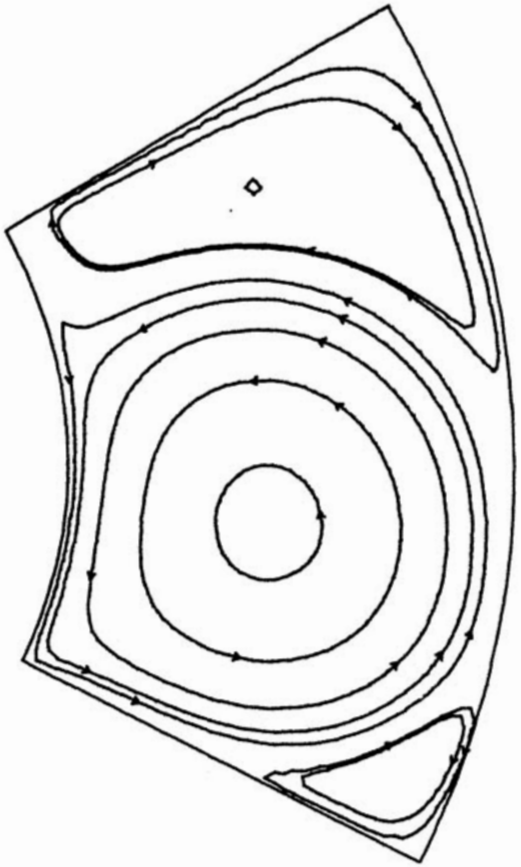

Figure 11. Computed streamline pattern for $Re = 2000$ on an 80 × 80 mesh. Second order

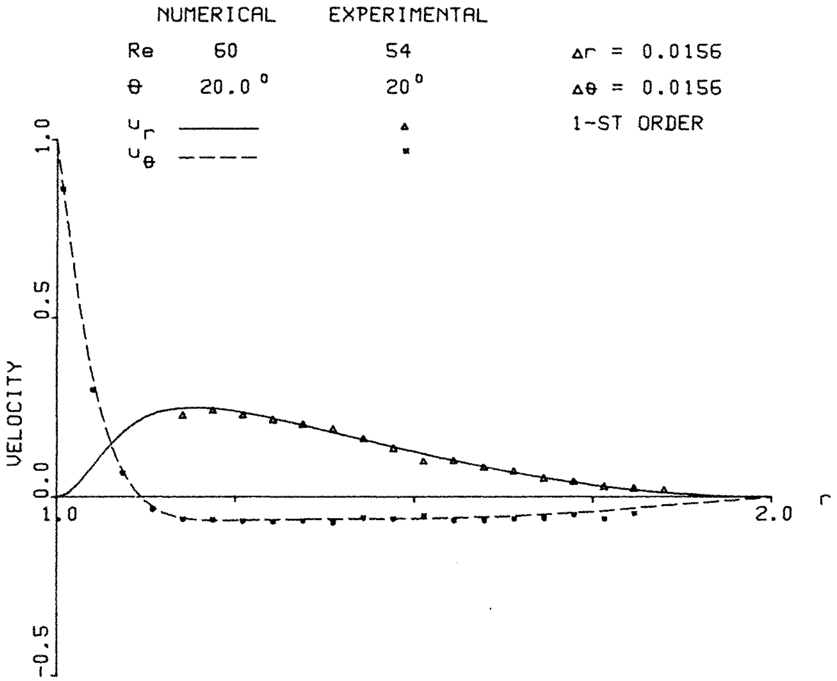

Figure 12. Numerical (upwind scheme on a 64 × 64 mesh) and experimental (for the plane $Z = 100$ mm) results along a radial line at $\theta = 20°$. $Re \cong 60$

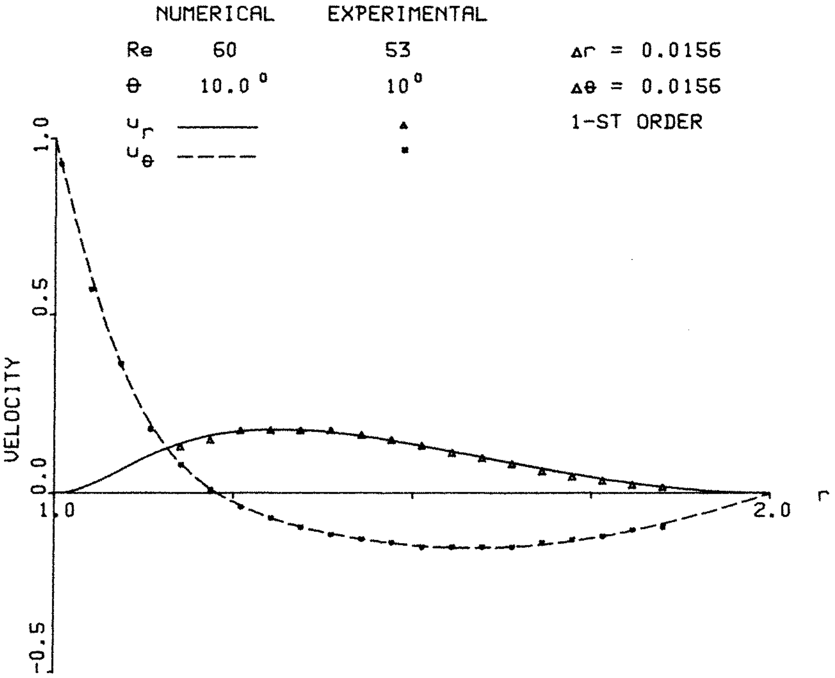

Figure 13. Numerical (upwind scheme on a 64 × 64 mesh) and experimental (for the plane $Z = 100$ mm) results along a radial line at $\theta = 10°$. $R \cong 60$

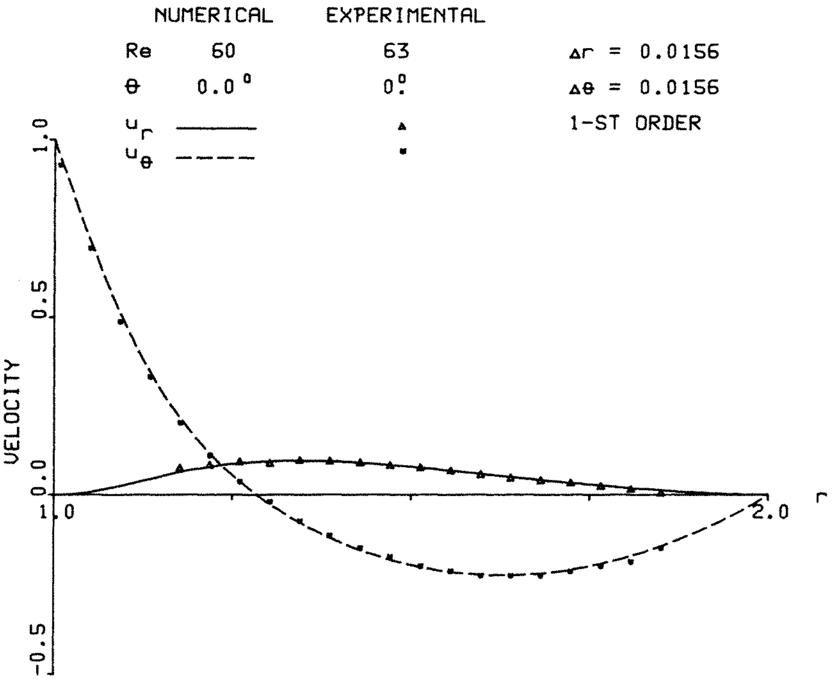

Figure 14. Numerical (upwind scheme on a 64 × 64 mesh) and experimental (for the plane $Z = 100$ mm) results along a radial line at $\theta = 0°$. $Re \cong 60$

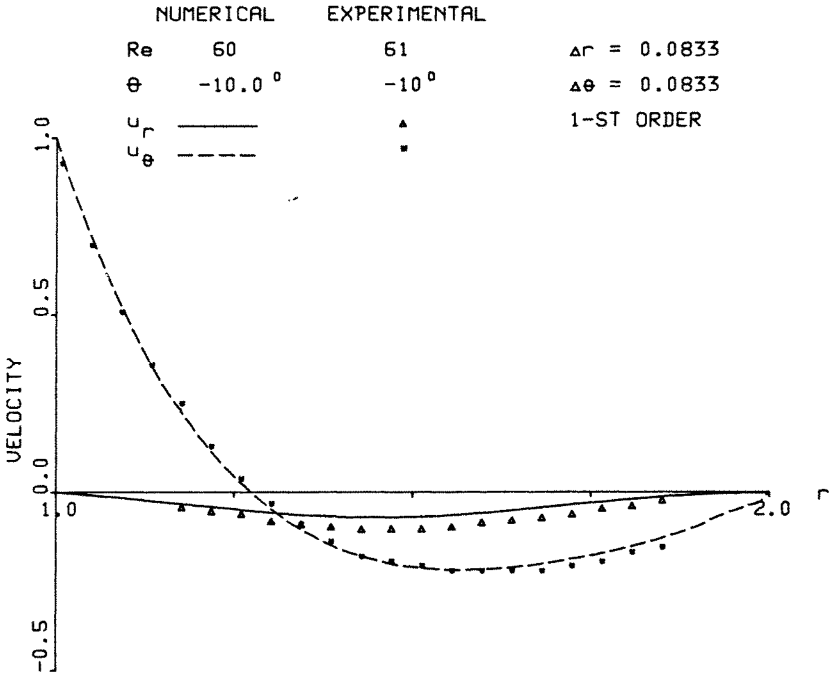

Figure 15. Numerical (upwind scheme on a 12 × 12 mesh) and experimental (for the plane $Z = 100$ mm) results along a radial line at $\theta = -10°$. $Re \cong 60$

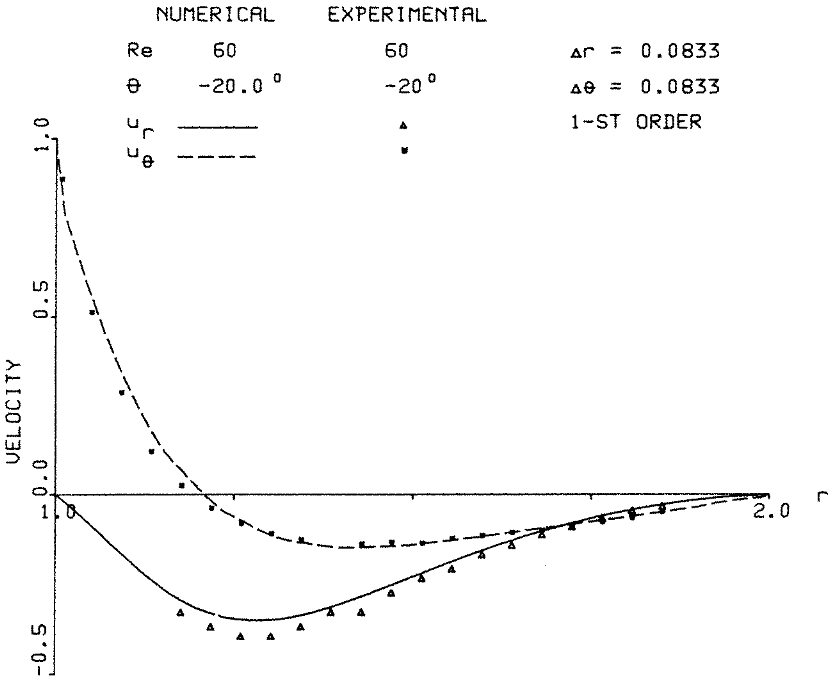

Figure 16. Numerical (upwind scheme on a 12 × 12 mesh) and experimental (for the plane $Z = 100$ mm) results along a radial line at $\theta = -20°$. $Re \cong 60$

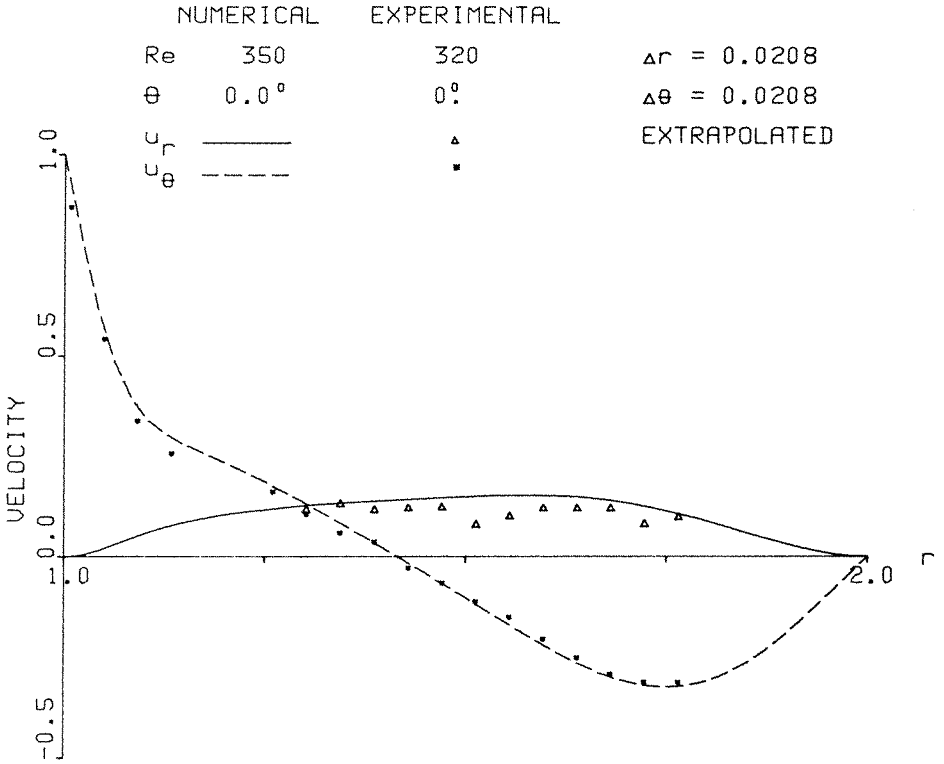

Figure 17. Numerical and experimental (for the plane $Z = 200$ mm) results along a radial line at $\theta = 0°$. $Re = 320$. The numerical values are obtained by extrapolating the solutions obtained on two grids: 48 × 48 and 96 × 96 intervals. (Compare the measured values with those in Figure 20 for the plane $Z = 100$ mm)

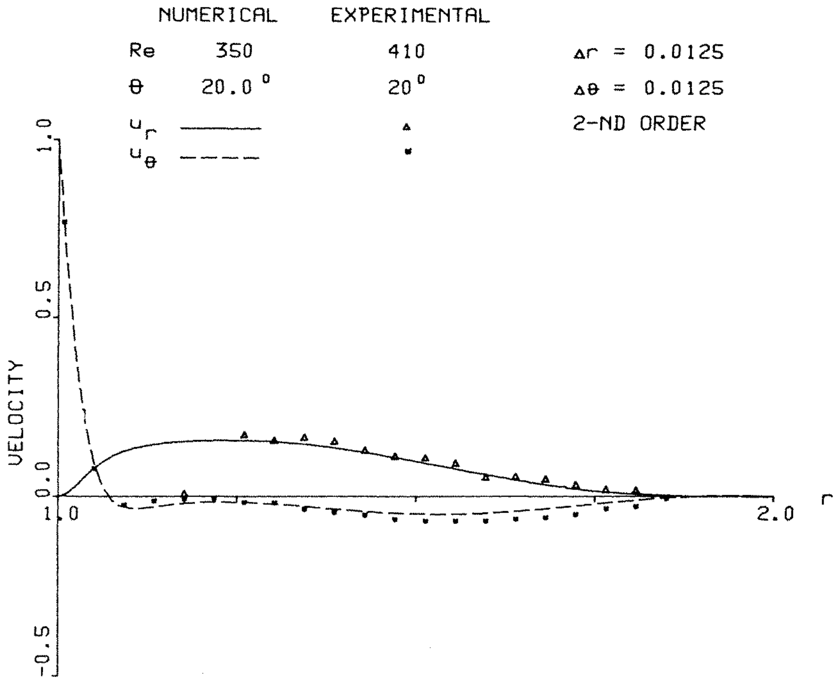

Figure 18. Numerical (second order scheme on a 80 × 80 mesh) and experimental ($Z = 100$ mm) results along a radial line at $\theta = 20°$. $Re \cong 350$

($\pm 20°$, $\pm 15°$, $\pm 10°$, $\pm 5°$ and 0°). It was found difficult to measure the velocity near the corners of the cavity and the region which could be measured at deeper cross-sections (such as the mid-plane at $Z = 200$ mm) was even more restricted. For this reason most measured results which are presented here are for a plane located closer to the end wall ($Z = 100$ mm; i.e. one-fourth of the cavity length). For the low *Re* group the flow at this cross-section is strictly two-dimensional (Figure 4), whereas for the higher *Re* group a well observed axial flow component is present (Figure 5). In the following, we show results for 5 of the measured angles: $\pm 20°$, $\pm 10°$ and 0°.

Figures 12–16 show the computed and the measured velocity components along a radial line for the five angles, for the low *Re* group. The numerical computations have been done on a relatively fine mesh (64 × 64 intervals) using upwinded FDE. The agreement between the numerical and the experimental results is very good for all the measured cases. A much coarser grid solution (12 × 12 intervals) with an estimated accuracy of about 5 per cent is almost as good as the one obtained on the finer grid. The large errors have been observed for $-20°$ and $-10°$. These cases are shown in Figures 15 and 16.

For the high *Re* group computed results have been obtained for a mean Reynolds number ($Re = 350$) and the extreme values of *Re* which have been registered during the experiments ($Re = 280$ and $Re = 410$). Comparison of numerical solutions obtained on successively refined grids shows that the accuracy of the upwinded FDE (3)–(5) is not adequate for this *Re* group and even on the finest meshes that we have used, the estimated relative error is about 10 per cent (Figure 3).

As mentioned before, a way of increasing accuracy is by extrapolation. By Table II extrapolations are meaningful in our computations. Extrapolated results [to $O(h^2)$ and $O(h^3)$], which have been computed by relatively fine grid solutions, agree well with each other. Such an extrapolated solution is compared with the measured velocity components in Figure 17. A

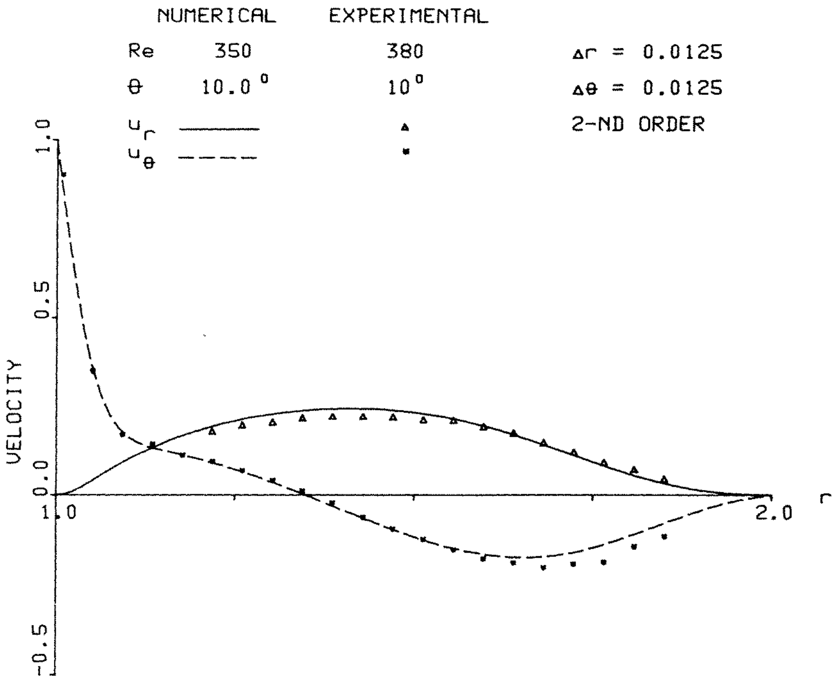

Figure 19. Numerical (second order scheme on a 80 × 80 mesh) and experimental ($Z = 100$ mm) results along a radial line at $\theta = 10°$. $Re \cong 350$

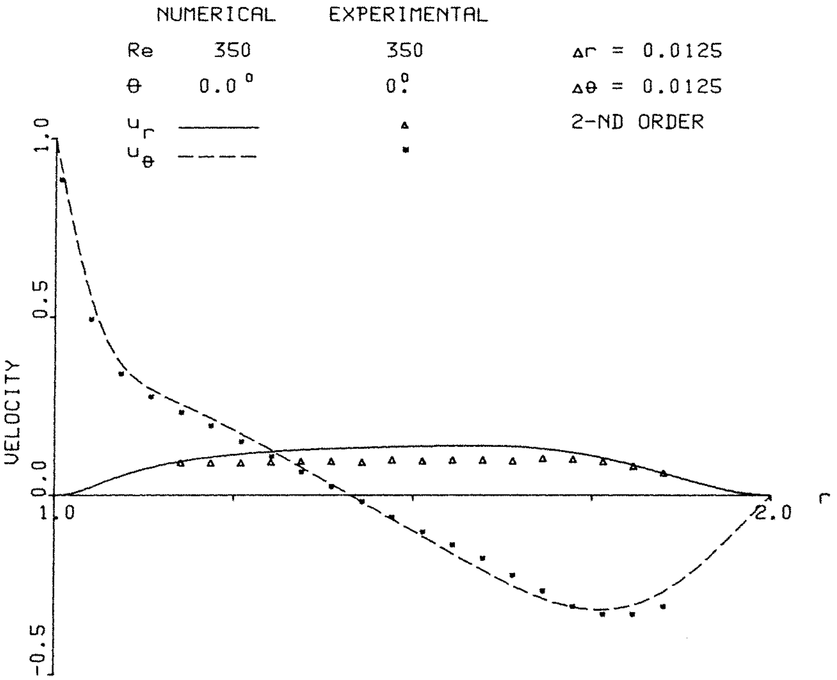

Figure 20. Numerical (second order scheme on a 80 × 80 mesh) and experimental ($Z = 100$ mm) results along a radial line at $\theta = 0°$. $Re \cong 350$

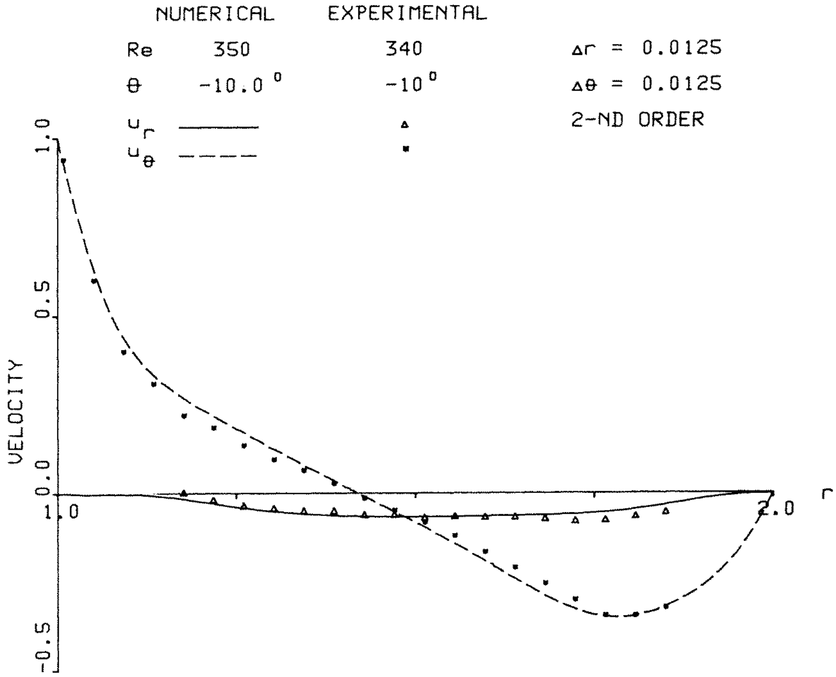

Figure 21. Numerical (second order scheme on a 80 × 80 mesh) and experimental ($Z = 100$ mm) results along a radial line at $\theta = -10°$. $Re \cong 350$

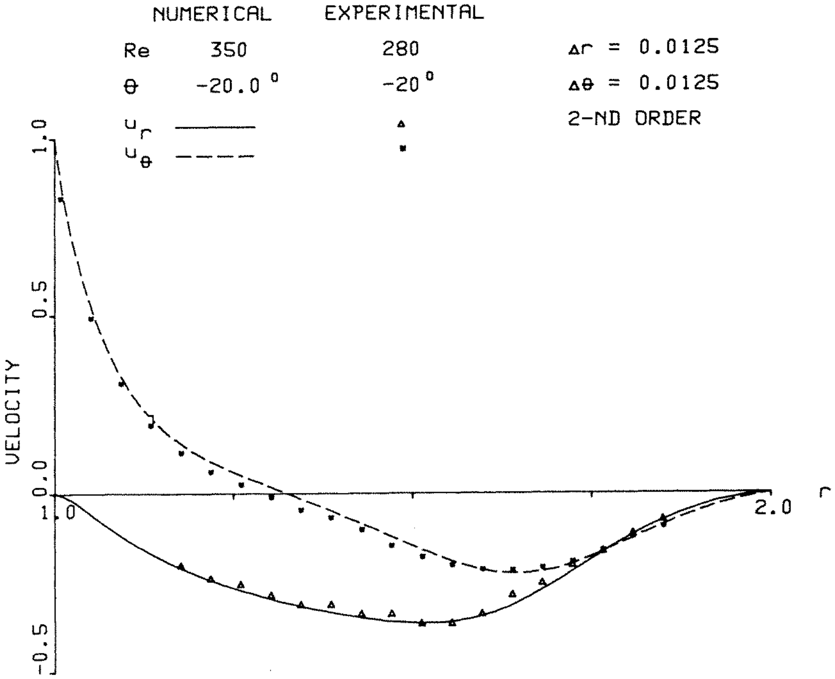

Figure 22. Numerical (second order scheme on a 80 × 80 mesh) and experimental ($Z = 100$ mm) results along a radial line $\theta = -20°$, $Re \simeq 350$

corresponding comparison between the solution to the central finite difference equations (on a mesh with 80 × 80 intervals), is shown in Figures 18–22. As can be observed there is a good agreement between the computed and the measured velocities. These Figures reveal that there are small disagreements in the azimuthal velocity component for some angles (Figures 19 and 20) and in the radial velocity component at 0°. For the last angle we have some measured values from the mid cross-section ($Z = 200\,\mathrm{mm}$) too. These measurements are compared with the computed velocity components in Figure 17. Most discrepancies which could be observed at this angle at the plane closer to the end wall, ($Z = 100\,\mathrm{mm}$, Figure 20), are absent.

CONCLUDING REMARKS

The flow in a two dimensional polar cavity has been considered numerically and experimentally. By considering the numerical solutions computed on different grids, the absolute levels of the accuracy could be estimated. It has been found that for the low *Re* group ($Re = 60$) the solution to the upwind FDE on coarse grids is accurate enough and it is in good agreement with the experimental results. For the higher *Re* group ($Re = 350$) only fine mesh solutions, using either central FDE or extrapolations, give comparable levels of accuracy. The validity of an extrapolated solution can be assessed by computing the truncation error functions and checking their independence on the mesh size. We have found that for valid extrapolations, solutions on fine meshes have to be computed. For a comparable accuracy similar grids have to be used with the second order FDE. In many cases extrapolations are preferable to a high order FDE, since iterative schemes associated with lower order methods often converge faster than the corresponding schemes for a higher order FDE.

Our experiments provided qualitative and quantitative results. The flow field was visualized, and the extent of the three-dimensional effects could be registered. By using a laser Doppler anemometer, we measured the velocity components at some sections of the cylindrical cavity. The measured velocity components were compared to the computed solutions. We have found very good agreement between the results. Small discrepancies have only been found for some angles in the high *Re* group. These small differences between the numerical and the experimental results are attributed to three-dimensional effects in the apparatus.

REFERENCES

1. S-Y. Tuann and M. D. Olson, 'Review of computing methods for recirculating flows', *J. Comp. Phys.*, **29,** 1–19 (1978).
2. M. M. Gupta and R. P. Manohar, 'Boundary approximation and accuracy in viscous flow computations', *J. Comp. Phys.*, **31,** 265–288 (1979).
3. R. Peyret and T. D. Taylor, *Computational Methods for Fluid Flow*, Springer Verlag, 1983.
4. R. Schreiber and H. B. Keller, 'Spurious solutions in driven cavity calculations', *J. Comp. Phys.*, **49,** 165–172 (1983).
5. F. Pan and A. Acrivos, 'Steady flows in rectangular cavities', *J. Fluid Mech.*, **28,** 643–655 (1967).
6. R. D. Mills, 'On the closed motion of a fluid in a square cavity', *J. Royal Aeronautical Soc.*, **69,** 116–120 (1965).
7. V. YA. Bogatyrev and A. V. Gorin, 'End effects in rectangular cavities', *Fluid Mechanics-Soviet Research*, **7,** (4), 101–106 (1978).
8. J. R. Kossef, R. L. Street, P. M. Gresho, C. D. Upson, J. A. C. Humphrey and W.-M. To, 'A three-dimensiional lid-driven cavity flow: experiments and simulation', in C. Taylor, J. A. Johnson and W. R. Smith (eds), *Numerical Methods in Laminar and Turbulent Flow*, Pineridge Press, 1983, pp. 564–581.
9. P. J. Roache, *Computational Fluid Dynamics*, Hermose Publishers, 1972.
10. T. Thunell and L. Fuchs, 'Numerical solution of the Navier–Stokes equations by multi-grid techniques', in C. Taylor and A. B. Schrefler (eds), *Numerical Methods in Laminar and Turbulent Flow*, Pineridge Press, 1981, pp. 141–152.
11. L. Fuchs, 'A fast numerical method for the solution of boundary value problems', *TRITA-GAD-4. The Royal Institute of Technology, Stockholm*, Sweden, 1980.
12. P. Buchhave, 'The measurement of turbulence with the burst-type laser-doppler anemometer—errors and correction methods', *Technical Report No. TRL-106, State University of New York at Buffalo*, 1979.
13. G. De Vahl Davis, 'Natural convection of air in a square cavity: a bench mark numerical solution', *Int. J. Num. Meth. Fluids*, **3,** 249–264 (1983).